A stochastic model for simulating the FC and ZFC processes of FE and PY particles

Um modelo estocástico para a realização de simulações dos processos de FC e ZFC de partículas de FE e PY

DOI:10.34115/basrv5n2-035

Recebimento dos originais: 03/03/2021
Aceitação para publicação: 13/04/2021

Rafael Santos da Costa
Graduando do Curso de Licenciatura em Matemática pela Universidade Federal do Pará
Instituição: Universidade Federal do Pará, Faculdade de Matemática - UFPA
Endereço: Rua Raimundo Santana Cruz, s/n, Bairro São Tomé, Salinópolis – PA, Brasil
E-mail: rafael_santos723@outlook.com

Thiago Rafael da Silva Moura
Doutor em Física Pela Universidade Federal do Rio Grande do Norte.
Instituição 1: Universidade Federal do Pará, Faculdade de Física – LabX - UFPA
Endereço: Rua Raimundo Santana Cruz, s/n, Bairro São Tomé, Salinópolis – PA, Brasil
Instituição 2: Universidade Federal do Sul e Sudeste do Pará, Programa de Pós-graduação em Propriedade Intelectual e Transferência de Tecnologia para Inovação – PROFNIT-Marabá – PA
Endereço: Folha 31, Quadra 7, Lote Especial - Nova Marabá, CEP: 68.507.590, Marabá-PA, Brasil
E-mail: trsmoura@yahoo.com.br

ABSTRACT

We performed computer simulations on the nanoscopic scale to find the energy distribution of the anisotropic barrier of Fe and Py nanoparticles. We investigated the physical properties of these magnetic nanoparticles for potential application in the catalysis of coal liquefaction. We examined the characteristics of the microstructure of these fundamental nanoparticles to optimize the ability to catalyze the breakdown of carbon-carbon bonds. We reported our results for nanoparticles, cubic, Fe and Py. We constructed ZFC and FC curves to determine the distribution of the blocking temperature. The ZFC and FC curves exhibit the same blocking temperature, behavior dependent on the magnitude of the applied magnetic field. Finite-scale scale effects determinant for technological applications are reported.

Keywords: Nanoparticles, Magnetism, Catalyst, Liquefaction, Coal.

RESUMO

Realizamos simulações computacionais na escala nanoscópica para encontrar a distribuição de energia da barreira anisotrópica de nanopartículas de Fe e Py. Investigamos propriedades físicas dessas nanopartículas magnéticas para potencial aplicação na catálise da liquefação de carvão. Prescrutamos as características da microestrutura dessas nanopartículas fundamentais para a otimização da capacidade de catalisar a quebra das ligações carbono-carbono. Reportamos nossos resultados para nanopartículas, cúbicas, de Fe e Py com 15, 25 e 35 nm de aresta. Construímos curvas ZFC e FC para determinar a distribuição da temperatura de bloqueio. As curvas ZFC e FC exibem a mesma temperatura de bloqueio, comportamento dependente magnitude do campo magnético aplicado. Efeitos de escala de tamanho finito determinantes para aplicações tecnológicas são reportados.

Palavras-chave: Nanopartículas, Magnetismo, Catalisador, Liquefação, Carvão.

1 INTRODUCTION

Nanoparticles are particles with dimensions between 1 and 100 nm, having a size between proteins and viruses, 1 nm and 100 nm, respectively [1]. Particles with these dimensions are the target of scientific, experimental and theoretical investigations, as they are important for industry with applications in transport, energy, environment, medicine, textile engineering, biotechnology and construction. A particular type of nanoparticles, mesoporous, have physico-chemical properties such as mechanical resistance, are chemically stable, have synthetic versatility and are biocompatible. There are two types of nanoparticles: organic and inorganic. In the subgroup of organic nanoparticles, the polymeric ones, used for medium applications, stand out dendrimers, have a branched structure formed by nuclei and multiple layers; liposomes, are formed by a double lipid layer that can be used to encapsulate hydrophilic and hydrophobic drugs; micelles, are colloidal aggregates formed by a hydrophobic inner part and a hydrophilic outer part. In the subgroup of inorganic nanoparticles we highlighted those of silica, they are synthesized with regular difficulty, obtaining different shapes and sizes, in addition they are biodegradable, inert and have a good biodistribution; the gold ones are metallic, with good optical and electrical properties that depend on their size and geometry; those of iron oxide, are biocompatible and biodegradable, especially those of magnetite, with high potential for application in biomedicine; quantum dots (QD), are used as probes for images, depending on the size, they can present high quantum yield, high photostability and high fluorescent emission; carbon nanotubes, are single layers in cylindrical shape, have a high specific surface that serves to anchor a diversity of therapeutic molecules

[1],[2]. Mesoporous nanoparticles are being applied in biomedicine, involving preparation and specific applications, to promote tools for human health; in metallic, metallic and organometallic systems; used in bioadsorption, enzyme immobilization, drug delivery, catalysis, hyperthermia, among other applications [1]-[33].

In addition, the production of miniaturized devices on the nanoscale, technology for recording data on permanent magnetic materials (non-volatile magnetic memory), spin valves, magnetic tunneling joints, study of fine magnetic particles as a catalyst in the coal liquefaction reaction and for applications in the treatment of cancer through the study of the phenomenon of magnetic hyperthermia, applications are strongly linked to modern nanomagnetism and spintronics. In nanomagnetism and spintronics, the study and development of new computational tools to prescribe the micromagnetic properties of these materials in the nano, micro and mesoscopic scales is urgent [34]-[43].

A promising branch of application of magnetic nanoparticles is for the development of catalysts. Several methods are being developed for the synthesis of nanomaterials, including methods with micro-emulsion, co-precipitation of iron ions in an alkaline medium, hydrothermal synthesis, deposition of nanoparticles on the surface by $Fe(NO_3)_3$ thermolysis, chemical vapor deposition, impregnation wet iron precursor followed by repeated cycles of oxidation and reduction to obtain magnetic nanoparticles [44]-[54].

Recent studies show that samples of iron nanoparticles, synthesized on a support of mesoporous silica, with deposition of a kind of Fe3+, followed by hydrogen reduction have catalytic activity. A nanoparticle based catalyst can have a catalytic activity six times greater than a conventional material and exhibit a strong selectivity for methane production. Critical properties dictate the rule in this type of system. Scale effects of finite size of the particles show that there is selectivity of methane to the size of the catalyst. The nanometric size of the particles serves as a severe limitation for accounting for how many carbon-containing species can be adsorbed onto a particle. Therefore, this phenomenon makes carbon chains less likely to collide and combine. Another determining factor is related to the size of the catalyst with the increase in the chemisorption of hydrogen, which leads to an additional termination of the chain at the expense of the growth of the chain [8]-[36].

The use of coal deposits to extract carbon chains as a chemical raw material to replace oil has long been a goal. To achieve this goal, a convenient and inexpensive method of dividing coal into low molecular weight components is needed. To achieve

this degradation under the mildest possible conditions, the choice of catalysts is critical. Iron-based catalysts can be produced cheaply enough to prevent this need. For these reasons, nanoscale iron (and its oxides) has been investigated as a candidate for coal liquefaction catalyst [36].

The liquefaction of coal is a physical phenomenon characterized by the breaking of carbon-carbon bonds. Experimental investigations show that iron is able to catalyze the formation of these bonds. In view of these experimental observations, we proposed to investigate the physical properties of iron and permalloy nanoparticles. We developed our computational model to observe ordinary physical properties of these nanoparticles. Our method is based on Monte Carlo methods. We developed our computational model based on the well-known Metropolis algorithm, coupling it with the theoretical development given for particles at the mesoscopic level [39] - [43]. We investigated the structural and magnetic properties of particles on the nanoscale (dimensions between 1 and 100 nm). We reported our results in this work.

2 THE THEORETICAL MODEL

We considered iron (Fe) and permalloy (Py) nanoelements with cubic geometry. We used simulation cells of 5 nm of edge. We started our model describing the energy density:

$$\begin{aligned} E = & \frac{A}{d^2}\sum_i \sum_j \hat{m}_i \cdot \hat{m}_j \\ & -K\sum_j \left(\hat{m}_j^x\right)^2 \\ & -\hat{H}\sum_j \hat{m}_j \\ & \frac{+Ms^2}{2}\sum_i \sum_j \left(\frac{\hat{m}_i \cdot \hat{m}_j}{r_{i,j}^3} - 3\frac{(\hat{m}_i \cdot \vec{r}_{i,j})(\hat{m}_j \cdot \vec{r}_{i,j})}{r_{i,j}^5}\right) \end{aligned} \quad (1)$$

the first term is exchange energy, it is A the exchange stiffness and d the edge of the simulation cell represented in figure 1, which involves interactions between adjacent cells of the nanoelement; the second term is uniaxial anisotropy energy: along the axis x, and K the uniaxial anisotropy constant, models the preferred magnetization direction along a specific axis; the third term is Zeeman energy: where $\vec{H} = H_x\hat{\imath}$ it is the magnetic field applied along the axis of easy magnetization, the response of the material in relation to an applied magnetic field; the fourth term describes dipolar energy: in this term Ms is the saturation magnetization of the material, it describes the long-range interaction between all the cells of the nanoelement. The set terms $\{\hat{m}_j\}$ are the magnetic moments of the simulation cells, which have a set of approximate atomic moments, in this model, for a

single magnetic moment of the simulation cell with $d = 5\ nm$. The magnetic constants for iron (Fe) and permalloy (Py) are shown in the table 1 [39]-[43].

Figure 1 - Schematic representation of (a) nanoelement and (b) simulation cell of the theoretical model.

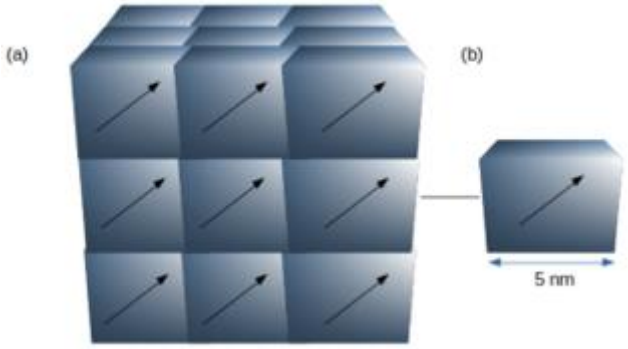

Table 1 - Macroscopic magnetic properties of the Fe and of Py

	Fe	Py
$A(J/m)$	$2{,}5 * 10^{-11}$	$1{,}3 * 10^{-11}$
$Ms(A/m)$	$1{,}7 * 10^{6}$	$0{,}8 * 10^{6}$
$K(J/m^3)$	$2{,}5 * 10^{-4}$	0

We performed micromagnetic simulations to obtain the measurements of the physical observables, estimating the observables concerning the solutions of the master equation:

$$\frac{dP(i,j)}{dt} = \sum_{i \neq j}\{W(i,j)P(j,t) - W(j,i)P(i,t)\} \qquad (2)$$

where $W(i,j)$ is the state's probability transition rate i for j and $P(j,t)$ is the state probability$j$ in the instant of time$t$. Given the transition rates, we found the stationary solution that satisfies the condition

$$\sum_{i \neq j}\{W(i,j)P(j,t) - W(j,i)P(i,t)\} = 0 \ (3)$$

The numerical solution of the master equation for the steady state (3) served as the basis for the development of the Metropolis algorithm [38]. The Metropolis algorithm is described below:

1. Configure an initial configuration j for the system;
2. Generate a tentative configuration of the i- th simulation cell;
3. If $\Delta E_{j,i} = E_j - E_i < 0$, the configuration i is accepted;

4. Otherwise, a random number is generated $r \in (0,1)$. If $r < P(\Delta E_{j,i}) \propto exp(\Delta E_{i,j}/K_B T)$ the new configuration is accepted.

5. Otherwise, the configuration j remains.

We used simulation cells with$d = 5\ nm$ of edge. We proceeded with the simulations of the treatments ZFC and FC with 10^7 Monte Carlo (PMC) steps. We estimated the physical observables for PMC values greater than $N = 10 * L^3$, the number of cells simulating the edge of the cubic nanoelement. When$N > 10 * L^3$, we observed the stabilization of the measures, therefore, after this threshold we calculated the moments of energy$\langle E \rangle$ and magnetization$\langle \vec{M} \rangle$. The expected values of the first moment of magnetization were estimated by the equation

$$\langle M \rangle = \sum_{i=1}^{N} p_i M_i = \frac{1}{N} \sum_{i=1}^{N} M_i \quad (4)$$

3 RESULTS AND DISCUSSION

Magnetization measures *zero-field-cooled* (ZFC) and *field-cooled* (FC) are dependent on temperature. Magnetization measurements using the ZFC and FC procedures are used to find the energy distributions of the barrier. To obtain a curve according to the ZFC procedure, the sample is cooled from a temperature T higher than the blocking temperature T_B with the applied magnetic field null $\vec{H} = 0$, state in which the particles are in a disordered state, in this case superparamagnetic. Upon reaching a temperature $T < T_B$ the nanoparticles are in the blocked state. Then, the heating process starts, a magnetic field is applied $\vec{H} \neq 0$ until it reaches a temperature (T) higher than the blocking temperature. Throughout this process, magnetization measurements are taken. The FC curve is obtained when the sample of nanoparticles, in the cooling and heating processes, is submitted to the same magnetic field$\vec{H} \neq 0$. To perform the ZFC and FC measurements, the applied magnetic field must be much smaller than the field related to anisotropy energy to ensure that the measurements reflect the energy distribution of the barrier.

We started our ZFC measurements at the initial temperature $T_0 = 290\ K$. At this temperature, the nanoparticles are in equilibrium in the superparamagnetic state. The magnetic field is kept null $\vec{H} = 0$, when the sample is cooled to the temperature of $T_F = 0.01\ K$. At this temperature, the magnetic field $\vec{H} \neq 0$ is applied while the sample is heated. Magnetic field values are 10, 20, 30, 40 and $50\ mT$. After the application of the field, the sample is projected to an out-of-balance state, quantified by the term of the

Zeeman energy in equation (1). Under these same conditions, temperature and magnetic field, the FC curves were constructed. Differentiating from the ZFC curves, the magnetization curve is obtained, both in the cooling and heating processes, with$\vec{H} \neq 0$. The samples are made of iron (Fe) and permalloy (Py). The geometry is cubic with edges (d) equal to 15, 25 and 35 nm.

In figures 2 and 3, we presented the first set of measures. To obtain the curves observed in figures Zero Field Cooled-(Fe) and Zero Field Cooled-(Py), ZFC curves, we fixed the sample size with $d = 15\ nm$. The sample is taken out of equilibrium with the magnetic field applied between $10 - 50\ mT$. We noted that the qualitative behavior of magnetization does not change. It grows, with a non-zero field, from $T = 0.01K$ to the thermodynamic equilibrium point (maximum point on the curve). At the thermodynamic equilibrium point, magnetization decreases as the temperature increases, according to Curie's law ($\propto 1/T$) measuring the measurements at the point $T = 290\ K$. In the FC curves, shown in figures Field Cooled-(Fe) and Field Cooled-(Py), the constant magnetic field is applied to the sample at $290\ K$, kept constant throughout the cooling process. In this process, the magnetization increases until it reaches the blocking temperature T_B. We observed that the magnetization remains fixed while the temperature decreases until $0.01K$. At this point, the sample is subjected to the heating process. The magnetization remains fixed until reaching T_B. At this point, typical measurements of magnetization are of its state of thermodynamic equilibrium. We highlighted, in figures 2 and 3, that for the ZFC curves; several maximum points were observed, depending on the magnitude of the magnetic field, for the FC curves; we observed the displacement, in the sense that the temperature increases, of the magnetization to higher values of the magnetic field. Therefore, we observed that the measure of the energy distributions of the barrier is dependent on the magnitude of the projection for the state out of balance by the Zeeman energy, third term of the equation (1).

Figure 2 - Curves Zero Field Cooled (Fe) and Field Cooled (Fe) of the cubic sample of the nanoelement of Fe with an edge equal to $d = 15nm$. The temperature (T) was varied from the $0{,}01 - 290K$. The applied magnetic field was varied from $10mT$ to $50mT$.

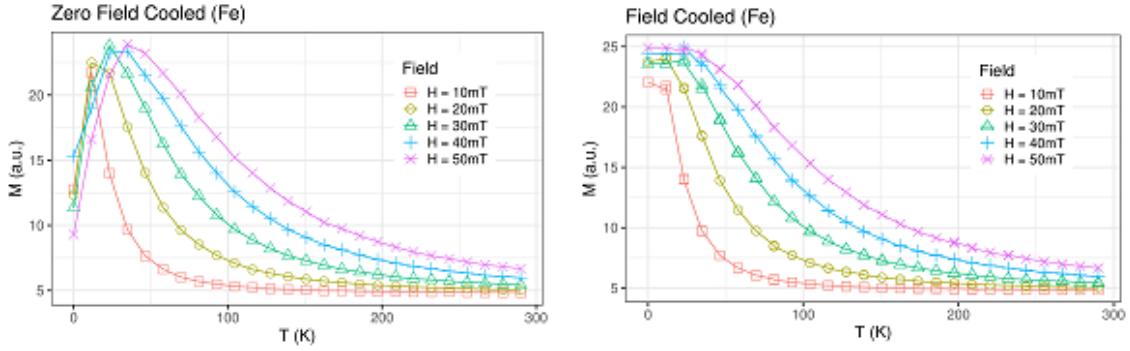

Figure 3 - Curves Zero Field Cooled (Py) and Field Cooled (Py) of the cubic sample of the permalloy nanoelement with an edge equal to $d = 15nm$. The temperature (T) was varied in the range of $0{,}01 - 290K$. The applied magnetic field was varied from $10mT$ to $50mT$.

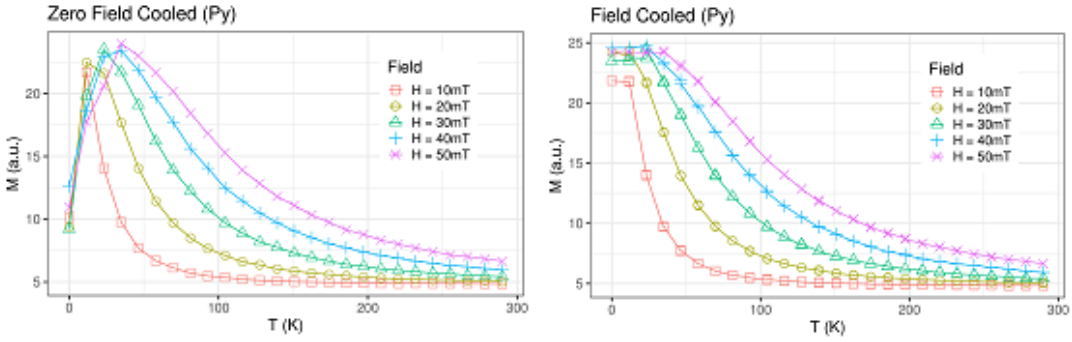

In figure 4, we presented typical magnetization measurements for the iron and permalloy nanoelements, called (Fe) and (Py), respectively. The samples chosen to display these results are those with edge. We noted that for $T < T_B$, the FC and ZFC curves exhibit different behaviors until reaching the temperature $T = T_B$, from which both curves show the same behavior. Presenting decrease of magnetization $\vec{M}$ with increasing temperature T. Therefore, we observed that the convergence point of the FC and ZFC curves provide us with information about the energy distribution of the barrier.

Figure 4 - Zero Field Cooled and Field Cooled curves of the magnetization obtained for cubic samples of the nanoelements of iron and permalloy (Fe) and *(*Py), respectively. The edges of the samples are equal to $d = 15nm$. The physical parameters of temperature (T) and applied magnetic field, were maintained with the following values of $0{,}01 - 300K$ and $50mT$, respectively.

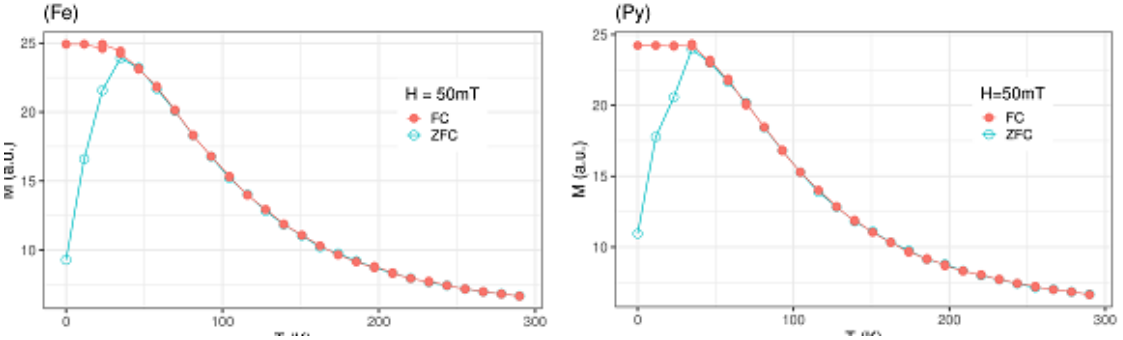

In the figure 5, typical magnetization FC measurements are shown for the Fe nanoelement. The normalized and non-normalized measurements, 5-[Field Cooled-Standard(Fe)] and 5-[Field Cooled-Normalized(Fe)], respectively. In figure 5-[Field Cooled-Standard(Fe)], we showed the non-normalized magnetization of nanoelements with edges equal to 15, 25 and 35 nm. In our numerical modeling, the magnetic nanoelement is divided into $D = N_x N_y N_z$; for the number of cells that make up the mesh, where magnetization is a function of, i.e.,$\vec{M}(D)$. To normalize the data shown in figure 5-[Field Cooled-Normalized(Fe)], we built an independent function of D, making $\vec{M}(D)/D = \vec{M}(Normalized)$. Thus, we normalized the HR measurements of the magnetization. As shown in figure 5-[Field Cooled-Normalized(Fe)], the curves will collapse into a single curve to $T \leq T_B$. For $T > T_B$, magnetization curves show similar behavior; diverging to the nanoelement with edge $d = 15nm$ and $T \cong 150K$. The nanoelement with edge $d = 15nm$ is the smallest sample we worked with, this behavior is expected due to the low dimensionality of the system, for which we expect greater fluctuations in the measurements of the physical observables. For larger nanoelements, stabilization of physical observables is expected with measurements made on larger samples. Therefore, this phenomenon is a consequence of the dimensions of the samples, i.e., finite-scale scale effects.

Figure 5 - Comparative measures of the magnetization for the FC treatment of cubic samples of the Fe nanoelement. FC curves [Field Cooled-Standard(Fe)] non-normalized and [Field Cooled-Normalized(Fe)] normalized. The edge sizes of the nanoelements are $d = 15$, $d = 25$ and $d = 35nm$. The applied magnetic field is of the order of and varying temperature from $0.01 - 290K$.

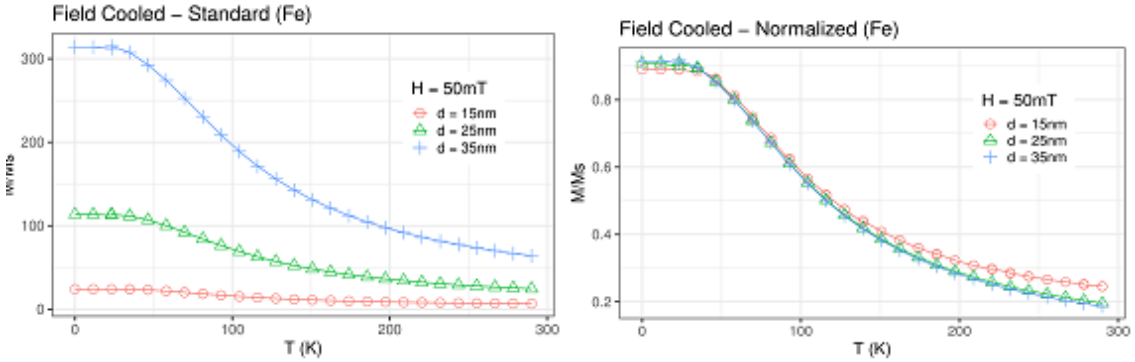

4 CONCLUSION

We presented results of our micromagnetic simulations for nanoparticles of Fe and Py. Nanoparticles have cubic geometry. The edge of the samples are, e.g. We built FC and ZFC curves to obtain the energy distributions of the anisotropic barrier. We concluded that, fixing the sample size and varying the applied magnetic field, a spectrum of maximums is obtained in the ZFC curve. In the FC curves, these points are the points for which the magnetization is a measure of the thermodynamic equilibrium, from which the magnetization decreases with increasing temperature. For each magnitude of the magnetic field, a blocking temperature is associated, which increases positively with the increase in the magnetic field. The FC and ZFC curves exhibit the same blocking temperature when the magnitude of the magnetic field and the dimension of the samples are kept fixed. Therefore, the ZFC or FC curve can be obtained to determine the blocking temperature. We noted that we can build a function for magnetization, as we did for the Fe samples, for which the FC curves converge. We observed that for the Fe sample with $d = 15nm$ the FC curve does not converge quantitatively, from the point $T \sim 150K$, for the new magnetization curve, but it has the same qualitative behavior. We intended to expand our results to estimate other physical quantities that optimize the liquefaction of coal, for example: for the increase of the catalytic reaction. Some of these properties are adsorption, chemisorption and blocking volume.

ACKNOWLEDGMENTS

We thank UFPA for financial support.

REFERENCES

1. Llinas, M.C.; Sánchez, D. Nanopartículas de sílice: Preparación y aplicaciones en biomedicina. Affinidad. 2014, LXXI, 20–31.

2. Deepak, T., Yashwant, P., Michel, D., Drugs and the pharmaceutical sciences vol. 166, Nanoparticulate Drug-Delivery Systems: An overview. Chapter 1. Nanoparticulate Drug-Delivery Systems: An Overview p.1-32. Edited by Deepak T., Michel D., Yashwant, P. (2007).

3. Huang, Y. Functionalization of mesoporous silica nanoparticles and their applications in organo-, metallic and organometallic catalysis. Ph.D. Thesis, Iowa State University, Ames, IA, USA, 2009.

4. Popat, A.; Hartono, S.B.; Stahr, F.; Liu, J.; Qiao, S.Z.; Qing Lu, G. Mesoporous silica nanoparticles for bioadsorption, enzyme immobilisation, and delivery carriers. Nanoscale 2011, 3, 2801–2818.

5. Sun, X. Mesoporous Silica Nanoparticles for Aplications in Drug Delivery and Catalysis. Ph.D. Thesis, Iowa State University, Ames, IA, USA, 2012.

6. Hoffmann, F.; Cornelius, M.; Morell, J.; Fröba, M. Silica-based mesoporous organic-inorganic hybrid materials. Angew. Chem. Int. Ed. 2006, 45, 3216–3251.

7. Slowing, I.I.; Vivero-Escoto, J.L.; Trewyn, B.G.; Lin, V.S.Y. Mesoporous silica nanoparticles: Structural design and applications. J. Mater. Chem. 2010, 20, 7924–7937.

8. Mirza-Aghayan, M.; Nazmdeh, S.; Boukherroub, R.; Rahimifard, M.; Tarlani, A.A.; Abolghasemi-Malakshah, M. Convenient and efficient one-pot method for the synthesis of 2-amino-tetrahydro-4H-chromenes and 2-amino-4H-benzo[h]-chromenes using catalytic amount of amino-functionalized MCM-41 in aqueous media. Synth. Commun. 2013, 43, 1499–1507.

9. Nale, D.B.; Rana, S.; Parida, K.; Bhanage, B.M. Amine functionalized MCM-41: An efficient heterogeneous recyclable catalyst for the synthesis of quinazoline-2,4(1H,3H)-diones from carbon dioxide and 2-aminobenzonitriles in water. Catal. Sci. Technol. 2014, 4, 1608–1614.

10. Nale, D.B.; Rana, S.; Parida, K.; Bhanage, B.M. Amine functionalized MCM-41 as a green, efficient, and heterogeneous catalyst for the regioselective synthesis of 5-aryl-2-oxazolidinones, from CO 2 and aziridines. Appl. Catal. A Gen. 2014, 469, 340–349.

11. Choudary, B.M.; Kantam, M.L.; Sreekanth, P.; Bandopadhyay, T.; Figueras, F.; Tuel, A. Knoevenagel and aldol condensations catalyzed by a new diamino-functionalized mesoporous material. J. Mol. Catal. A Chem. 1999, 142, 361–365.

12. Wu, N.; Li, B.; Liu, J.; Zuo, S.; Zhao, Y. Preparation and catalytic performance of a novel highly dispersed bifunctional catalyst Pt@Fe-MCM-41. RSC Adv. 2016, 6, 13461–13468.

13. Borodina, E.; Karpov, S.I.; Selemenev, V.F.; Schwieger, W.; Maracke, S.; Fröba, M.; Rößner, F. Surface and texture properties of mesoporous silica materials modified by silicon-organic compounds containing quaternary amino groups for their application in base-catalyzed reactions. Microporous Mesoporous Mater. 2015, 203, 224–231.

14. Trisunaryanti, W.; Dwi Putri, A.; Lutfiana, A.; Dewi, K. Transesterification of Waste Cooking Oil Using NH 2 /MCM-41 Base Catalyst: Effect of Methanol/Oil Mole Ratio And Catalyst/Oil Weight Ratio towards Conversion of Ester. Asian J. Chem. 2018, 30, 953–957.

15. Vekariya, R.H.; Prajapati, N.P.; Patel, H.D. MCM-41-anchored sulfonic acid (MCM-41-SO 3 H): An efficient heterogeneous catalyst for green organic synthesis. Synth. Commun. 2016, 46, 1713–1734.

16. Luštická, I.; Vrbková, E.; Vyskočilová, E.; Paterová, I.; Červený, L. Acid functionalized MCM-41 as a catalyst for the synthesis of benzal-1,1-diacetate. React. Kinet. Mech. Catal. 2013, 108, 205–212.

17. Alinasab Amiri, A.; Javanshir, S.; Dolatkhah, Z.; Dekamin, M.G. SO3H-functionalized mesoporous silica materials as solid acid catalyst for facile and solvent-free synthesis of 2H-indazolo[2,1-b]phthalazine-1,6,11-trione derivatives. New J. Chem. 2015, 39, 9665–9671.

18. Safaei, S.; Mohammadpoor-Baltork, I.; Khosropour, A.R.; Moghadam, M.; Tangestaninejad, S.; Mirkhani, V. SO3H-functionalized MCM-41 as an efficient catalyst for the combinatorial synthesis of 1H-pyrazolo-[3,4-b]pyridines and spiro-pyrazolo-[3,4-b]pyridines. J. Iran. Chem. Soc. 2017, 14, 1583–1589.

19. Kaiprommarat, S.; Kongparakul, S.; Reubroycharoen, P.; Guan, G.; Samart, C. Highly efficient sulfonic MCM-41 catalyst for furfural production: Furan-based biofuel agent. Fuel 2016, 174, 189–196.

20. Karnjanakom, S.; Kongparakul, S.; Chaiya, C.; Reubroycharoen, P.; Guan, G.; Samart, C. Biodiesel production from Hevea brasiliensis oil using SO 3 H-MCM-41 catalyst. J. Environ. Chem. Eng. 2016, 4, 47–55.

21. Sarrafi, Y.; Mehrasbi, E.; Mashalchi, S.Z. MCM-41-SO 3 H: An efficient, reusable, heterogeneous catalyst for the one-pot, three-component synthesis of pyrano[3,2-b]pyrans. In Research on Chemical Intermediates; Springer:Dordrecht, The Netherlands, 2015; pp. 1–13.

22. Appaturi, J.N.; Selvaraj, M.; Abdul Hamid, S.B.; Bin Johan, M.R. Synthesis of 3-(2-furylmethylene)-2,4-pentanedione using DL-Alanine functionalized MCM-41 catalyst via Knoevenagel condensation reaction. Microporous Mesoporous Mater. 2018, 260, 260–269.

23. Vrbková, E.; Vyskočilová, E.; Červený, L. Functionalized MCM-41 as a catalyst for the aldol condensation of 4-isopropylbenzaldehyde and propanal. React. Kinet. Mech. Catal. 2015, 114, 675–684.

24. Sharma, K.K.; Asefa, T. Efficient bifunctional nanocatalysts by simple postgrafting of spatially isolated catalytic groups on mesoporous materials. Angew. Chem. Int. Ed. 2007, 46, 2879–2882.

25. AJAYAN, Pulickel Madhavapanicker. Nanotubes from carbon. Chemical reviews, v. 99, n. 7, p. 1787-1800, 1999.

26. BAIBICH, Mario Norberto et al. Giant magnetoresistance of (001) Fe/(001) Cr magnetic superlattices. Physical review letters, v. 61, n. 21, p. 2472, 1988.

27. BINASCH, Grünberg et al. Enhanced magnetoresistance in layered magnetic structures with antiferromagnetic interlayer exchange. Physical review B, v. 39, n. 7, p. 4828, 1989.

28. BINDER, K.; LANDAU, David P. . A Guide to Monte-Carlo Simulations in Statistical Physics. 3rd ed. Cambridge: Cambridge University Press, 2009.

29. CARBONE, C.; ALVARADO, S. F. Antiparallel coupling between Fe layers separated by a Cr interlayer: Dependence of the magnetization on the film thickness. Physical Review B, v. 36, n. 4, p. 2433, 1987.

30. CINTRA, Murilo Bicudo et al. Magnetic resonance imaging: dynamic contrast enhancement and diffusion-weighted imaging to identify malignant cervical lymph nodes. Radiologia brasileira, v. 51, n. 2, p. 71-75, 2018.

31. GRÜNBERG, PETER et al. Layered magnetic structures: Evidence for antiferromagnetic coupling of Fe layers across Cr interlayers. Physical review letters, v. 57, n. 19, p. 2442, 1986.

32. HAYEK, S. et al. Application of nanomagnetic particles in hyperthermia cancer treatment. Nanotech, v. 2, p. 67-70, 2006.

33. Santos et al, R.. The relativistic effect of critical temperature reduction in the two dimensional Ising model. Braz. Ap. Sci. Rev, Curitiba, v. 4, n. 3, p. 1535-1543.

34. HINCHEY, Laura Lee; MILLS, D. L. Magnetic properties of superlattices formed from ferromagnetic and antiferromagnetic materials. Physical Review B, v. 33, n. 5, p. 3329, 1986.

35. HUBER, Dale L. Synthesis, properties, and applications of iron nanoparticles. Small, v. 1, n. 5, p. 482-501, 2005.

36. MARTÍNEZ-EDO, Gabriel et al. Functionalized ordered mesoporous silicas (MCM-41): Synthesis and applications in catalysis. Catalysts, v. 8, n. 12, p. 617, 2018.

37. MARTINS JR, S. M. S. B. et al. Excitations of interface pinned domain walls in constrained geometries. AIP Advances, v. 8, n. 5, p. 056004, 2018.

38. MUELA, Alicia et al. Optimal parameters for hyperthermia treatment using biomineralized magnetite nanoparticles: theoretical and experimental approach. The Journal of Physical Chemistry C, v. 120, n. 42, p. 24437-24448, 2016.

39. METROPOLIS, Nicholas et al. Equation of state calculations by fast computing machines. The journal of chemical physics, v. 21, n. 6, p. 1087-1092, 1953.

40. PEDROSA, S. S. et al. Dipolar effects on the magnetic phases of superparamagnetic clusters. Journal of Applied Physics, v. 123, n. 23, p. 233902, 2018.

41. SHINJO, Teruya (Ed.). Nanomagnetism and spintronics. Elsevier, 2013.

42. TANENBAUM, L. N.. Contrast enhancement in MR imaging: New options, new techniques, new opportunities. The Journal of Practical Medical Imagin and Management, 2015.

43. A. S. M. Silva, Ana L. Dantas, G. O. G. Rebouças, and A. S. Carriço. Nucleation of vortex pairs in exchange biased nanoelements. Journal of Applied Physics 109, 07D314, 2011.

44. Gotić, M.; Jurkin, T.; Musić, S. Factors that may influence the micro-emulsion synthesis of nanosize magnetite particles. Colloid Polym. Sci. 2007, 285, 793–800.

45. Zhou, Z.H.; Wang, J.; Liu, X.; Chan, H.S.O. Synthesis of Fe 3 O 4 nanoparticles from emulsions. J. Mater. Chem. 2001, 11, 1704–1709.

46. Yu, W.W.; Falkner, J.C.; Yavuz, C.T.; Colvin, V.L. Synthesis of monodisperse iron oxide nanocrystals by thermal decomposition of iron carboxylate salts. Chem. Commun. 2004, 20, 2306–2307.

47. Nedkov, I.; Merodiiska, T.; Slavov, L.; Vandenberghe, R.E.; Kusano, Y.; Takada, J. Surface oxidation, size and shape of nano-sized magnetite obtained by co-precipitation. J. Magn. Magn. Mater. 2006, 300, 358–367.

48. Utkan, G.G.; Sayar, F.; Batat, P.; Ide, S.; Kriechbaum, M.; Pişkin, E. Synthesis and characterization of nanomagnetite particles and their polymer coated forms. J. Colloid Interface Sci. 2011, 353, 372–379.

49. Mizutani, N.; Iwasaki, T.; Watano, S.; Yanagida, T.; Tanaka, H.; Kawai, T. Effect of ferrous/ferric ions molar ratio on reaction mechanism for hydrothermal synthesis of magnetite nanoparticles. Bull. Mater. Sci. 2008, 31, 713–717.

50. Daou, T.J.; Pourroy, G.; Bégin-Colin, S.; Grenèche, J.M.; Ulhaq-Bouillet, C.; Legaré, P.; Bernhardt, P.; Leuvrey, C.; Rogez, G. Hydrothermal Synthesis of Monodisperse Magnetite Nanoparticles. Chem. Mater. 2006, 18, 4399–4404.

51. Zhang, H.; Zhong, X.; Xu, J.-J.; Chen, H.-Y. Fe 3 O 4 /Polypyrrole/Au Nanocomposites with Core/Shell/Shell Structure: Synthesis, Characterization, and Their Electrochemical Properties. Langmuir 2008, 24, 13748–13752.

52. Bourlinos, A.B.; Simopoulos, A.; Boukos, N.; Petridis, D. Magnetic modification of the external surfaces in the MCM-41 porous silica: Synthesis, characterization, and functionalization. J. Phys. Chem. B 2001, 105, 7432–7437.

53. Arruebo, M.; Ho, W.Y.; Lam, K.F.; Chen, X.; Arbiol, J.; Santamaría, J.; Yeung, K.L. Preparation of Magnetic Nanoparticles Encapsulated by an Ultrathin Silica Shell via Transformation of Magnetic Fe-MCM-41. Chem. Mater. 2008, 20, 486–493.

54. Zhang, L.; Papaefthymiou, G.C.; Ying, J.Y. Synthesis and Properties of γ-Fe 2 O 3 Nanoclusters within Mesoporous Aluminosilicate Matrices. J. Phys. Chem. B 2001, 105, 7414–7423.